Single-photon emission radioactive particle tracking method for hydrodynamic evaluation of multi-phase flows

van der Sande, P. Christian; de Mooij, Jack; Wagner, Evert C.; Meesters, Gabrie M.H.; van Ommen, J. Ruud

DOI
10.1016/j.partic.2023.10.001

Publication date
2025

Document Version
Final published version

Published in
Particuology

Particuology 101 (2025) 43–56

Contents lists available at ScienceDirect

Particuology

journal homepage: www.elsevier.com/locate/partic

Single-photon emission radioactive particle tracking method for hydrodynamic evaluation of multi-phase flows

P. Christian van der Sande*, Jack de Mooij, Evert C. Wagner, Gabrie M.H. Meesters, J. Ruud van Ommen*

Department of Chemical Engineering, Delft University of Technology, Van der Maasweg 9, Delft 2629HZ, The Netherlands

ARTICLE INFO

Article history:
Received 10 July 2023
Received in revised form
6 October 2023
Accepted 7 October 2023
Available online 26 October 2023

Keywords:
Radioactive particle tracking
Granular flows
Hydrodynamics
Non-invasive monitoring
Horizontal stirred bed reactors

ABSTRACT

Evaluation of the hydrodynamics of opaque multi-phase flows remains a challenging task, with implications for various industrial processes such as chemical processing, pharmaceutical, and mineral processing. Understanding how design and operational variables affect the complex behavior of multi-phase flow systems is essential for optimizing processing conditions and improving efficiency. Radioactive particle tracking (RPT) has been a proven measurement technique to evaluate hydrodynamics in multi-phase flow systems. However, a limitation of the classical RPT technique exists in the assumptions made in the simulation of the count rate received by the detectors in correcting for varying flow-induced fluctuations in the volume fraction of the dispersed phase, often encountered in industrial multi-phase flow systems.

In this paper, we introduce a fundamentally novel experimental RPT method that directly uses detected incident photon hit locations for the reconstruction of the three-dimensional radioactive tracer particle position. We argue that this approach is inherently more robust as varying attenuation does not affect the reconstruction. The RPT setup consists of three identical γ-radiation slit collimator detectors that are placed equidistantly at 120° intervals. A subsequent calibration-experimentation procedure is established that allows reconstruction of the tracer particle position with spatial accuracy and precision in the order of 1 mm. We demonstrate the applications of this technique in evaluating hydrodynamics in multi-phase systems by characterizing the flow field of industrial-grade polypropylene reactor powder in a laboratory-scale horizontal stirred bed reactor.

1. Introduction

Multi-phase flows are widely encountered in various process industries such as chemical processing, petroleum refining, food processing, pharmaceutical, and mineral processing. Accurate modeling of hydrodynamics within multi-phase flow systems is essential for effective process design, scale-up, and optimization. However, current models include assumptions on particle and equipment scale that require experimental validation, preferably through non-invasive methods (Duduković, 2000). Traditional non-invasive optical techniques are not suitable for studying multi-phase flows with a large fraction of the particulate phase, often encountered in industrial applications, since the dense flows are opaque to visible light.

To overcome this limitation, non-invasive radiation-based techniques were developed to study multi-phase flow systems by tracking a single particle. These techniques, namely radioactive particle tracking (RPT), positron emission particle tracking (PEPT) (Parker et al., 1995; Stellema et al., 1998), and X-ray particle velocimetry (Kertzscher et al., 2004; Seeger et al., 2003), were inspired by medical research. They involve introducing a single radiation-emitting or absorbing tracer particle, which is dynamically similar to the dispersed phase, into the system of interest. Detectors located around the system calculate the tracer particle's position time series through inverse reconstruction within an accuracy in the order of 1 mm (Rasouli et al., 2015; Windows-Yule et al., 2020). The acquired position time series allows for evaluating the hydrodynamic properties of interest.

* Corresponding authors.
E-mail addresses: P.C.vanderSande@tudelft.nl (P.C. van der Sande), J.R.vanOmmen@tudelft.nl (J.R. van Ommen).

https://doi.org/10.1016/j.partic.2023.10.001

In the case of RPT, the tracer particle contains radioactive material that emits γ-radiation of constant energy in all directions. RPT offers the advantage of using a wide selection of available tracer isotopes with characteristic photon energy, such as Sc-46, I-131, Cs-137, or Au-198 (Upadhyay et al., 2019). This allows for the development of tailored tracer particles that emit γ-radiation with an optimal photon energy for specific experimental conditions. This is an advantage over PEPT, which involves positron-electron annihilation photons with a fixed energy of 511 keV. X-ray particle velocimetry, on the other hand, utilizes X-ray imaging or tomography and provides simultaneous information on gas-solid distribution and single-particle dynamics. However, it requires tracer particles with a large, high-density core to induce sufficient X-ray absorption. In contrast, the mass of tracer isotope material embedded in an RPT tracer particle can be significantly lower. This characteristic facilitates the development of a tracer particle that is dynamically similar to the dispersed phase.

Generally speaking, RPT experimentation involves two successive steps: a calibration procedure and an experimental measurement. During the calibration procedure, the tracer particle is positioned at numerous known positions within the system of interest. The obtained calibration data set is then utilized to accurately reconstruct the tracer's position during the subsequent experimental measurement. In the experimental measurement phase, the tracer particle is introduced into the system, and the time-resolved tracer particle position time series is reconstructed (Roy, 2017).

Pioneering efforts in space-resolved three-dimensional RPT or computer-aided radioactive particle tracking (CARPT) were made by Lin et al. (Lin et al., 1985). They developed photon-counting instrumentation that utilized the relationship between γ-ray intensity and the distance between the particle and the detector. The conventional setup consisted of twelve 51 $\times$ 51 mm sodium iodide scintillation detectors arranged in a staggered configuration. A Sc-46 ball coated with epoxy was used as the tracer particle to study re-circulation patterns in gas-fluidized beds. Before experimentation, an in situ calibration procedure was performed to establish a monotonic relationship between the count rate and the distance of the tracer to each detector. Devanathan et al. (Devanathan et al., 1990) refined the method by extending the number of detectors to sixteen and used it to investigate liquid circulation and turbulence in bubble columns. They employed a Sc-46 core embedded in a 2.4 mm polypropylene sphere with an air gap as a neutrally buoyant tracer particle. From the acquired tracer particle positions, Lagrangian auto-correlations, integral time scales, and radial and axial turbulent dispersion coefficients were computed.

In subsequent years, the established method was utilized in various studies to investigate flow fields in fluidized beds and bubble columns (Moslemian et al., 1992), spouted beds (Roy et al., 1994), three-phase fluidized beds (Larachi, Cassanello, et al., 1995), liquid fluidized beds (Larachi, Lord, et al., 1995, pp. 385–392), Larachi, Lord, et al., 1995irculating fluidized bed risers (Godfroy et al., 1996), and stirred tanks (Chaouki et al., 1997; Rammohan et al., 2001). Efforts were made by Duduković (Duduković, 2000) to further improve the spatial accuracy and precision by doubling the number of detectors to 32. They also employed a calibration procedure where the tracer was positioned at 1000 known in situ positions while recording the intensity obtained at each detector. This established approach utilizes an overabundance of detectors and employs a weighted least-squares method to calculate the tracer's position (Chaouki et al., 1997). This approach uses significantly more detectors than the suggested minimum of three. Although improving the precision of the measurement, using a larger number of detectors, along with the associated electronic hardware, significantly increases the cost and complexity of RPT experimentation (Roy et al., 2002).

RPT experimentation has found various applications in chemical reactor engineering research in recent years (Alizadeh et al., 2013; Dubé et al., 2014; Fraguío et al., 2007; Guha et al., 2007; Jain et al., 2017; Kalo et al., 2019; Rasouli et al., 2015; Roy et al., 2005). Despite the growing interest in RPT, the fundamentals and design parameters for the method have not undergone significant changes (Upadhyay et al., 2019). Instead, efforts have been focused on improving the reconstruction methodology in terms of spatial accuracy and precision, computational time, and its ability to cope with fast fluctuations in volume fraction, which are often encountered in multi-phase flow systems. Through an analytic approach, Monte Carlo simulations have been widely used in classical RPT experimentation to analyze the accuracy and improve the reconstruction methodology (Larachi, Chaouki, & Kennedy, 1995; F et al., 1994). Several improvements have been made to the Monte Carlo method, for example, the method was extended with a Real Coded Genetic Algorithm to reduce computational time (Yadav et al., 2017). Furthermore, machine learning methods have been proposed to improve reconstruction accuracy and computation time. Godfroy et al. (Godfroy et al., 1997) demonstrated in an earlier study that a feed-forward neural network can contribute to extremely fast position calculations. Recently, Yadav et al. (Yadav et al., 2020) showed that reconstruction algorithms based on support vector regression (SVR) and relevance vector regression (RVR) promote accurate position reconstruction.

In this work, we introduce a fundamentally novel experimental radioactive particle tracking method that allows reconstruction based on the photon hit location on a two-dimensional scintillation crystal detector plate, instead of classical RPT reconstruction based on the count rate. Therefore, we aim to improve RPT experimentation through a physical approach. We argue that the introduced method is inherently more robust, as varying attenuation caused by flow-induced fluctuations in volume fraction of the dispersed phase, such as those caused by rising bubbles between the tracer particle and detector, does not affect the reconstruction. As a result, it circumvents the need for extensive Monte Carlo dose-rate simulations or neural network optimization to cope with fast fluctuations in volume fraction. Section 2 describes the RPT setup and reconstruction methodology. Subsequently, the reconstruction results are presented and discussed in Section 3. To demonstrate the potential applications of the technique, an RPT case study with a horizontal stirred bed reactor is presented in Section 4. Finally, the work is summarized, and concluding remarks are provided in Section 5.

2. Experiments and methodology

2.1. Experimental setup

The RPT technique developed in this work is based on the Single Photon Emission Computed Tomography (SPECT) technique, which is commonly used in the medical field (Holman & Tumeh, 1990). The RPT setup consists of three identical γ-radiation detectors that are equidistantly placed around a field of view (FOV) at approximately 120° intervals, as depicted in Fig. 1.

Each detector comprises a casing, a slit collimator made of lead shielding plates and spacers, a scintillation crystal, and photomultiplier tubes, as depicted in Fig. 2. The detector casing is constructed with 6 mm lead covered with 3 mm stainless steel. The slit collimator height, which refers to the distance between the lead shielding plates, can be adjusted using spacers of varying heights (1, 2, or 4 mm) to control the amount of γ-radiation that passes

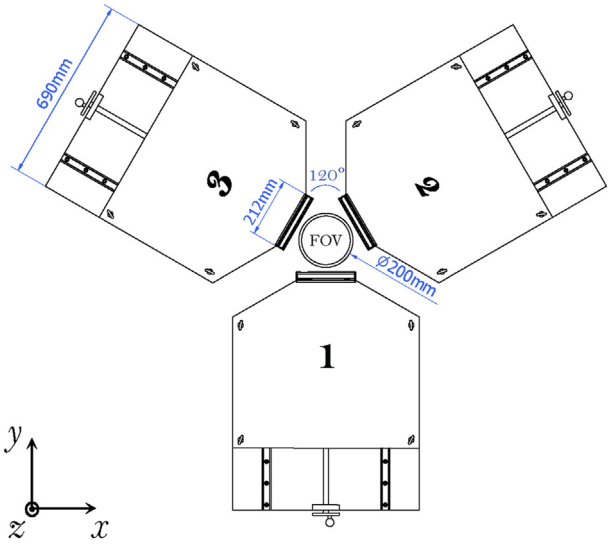

Fig. 1. Top view representation of the RPT setup. The three detectors are placed equidistantly around a FOV at approximately 120° intervals.

through the collimator. In this study, the detectors are equipped with a single slit positioned near the top of the lead shielding, measuring 212 mm in length and 4 mm in height, resulting in a high signal intensity at the scintillation crystal. The lead shielding plates have a thickness of 25 mm, effectively attenuating the γ-radiation that hits them. The scintillation crystals have a size of 550 × 550 mm and are coupled to an array of photomultiplier tubes (PMTs) that convert the detected γ-radiation to an amplified measurable electrical signal. The detectors are sensitive to γ-radiation with photon energies up to 600 keV.

The detectors have a detection efficiency that is the result of two components. The first component is the intrinsic detector efficiency, which is the ratio of the incident γ-photons and registered photons. The detector efficiency is dependent on the energy of the incident photons and thus differs for various tracer isotopes. The second component is the geometrical efficiency. Due to the slit collimators only a fraction of the emitted photon reaches the scintillation crystal. The geometrical efficiency is expressed as the ratio of the solid angle of the slit and the solid angle of a full sphere. The absolute detection efficiency is the multiplication of the detector and geometrical efficiency. The scintillation crystals can be translated forward or backward relative to the collimator to alter the magnification of the projection. If the crystal is moved closer to the collimator, the magnification is decreased. Conversely, if the crystal is moved farther away from the collimator, the magnification is increased. The current setup configuration has the scintillation crystal positioned at a distance of 400 mm from the slit collimator, allowing for the desired FOV to be captured.

In this work, two radioactive tracer particles were used for calibration-validation and experimentation purposes, respectively. The tracer particles were manufactured by embedding 1.6 mg gold in a 1.8 mm polystyrene bead. The increased mass of the tracer by inserting the gold core was compensated for by leaving an air pocket in the particle. Following neutron irradiation at the Reactor Institute Delft the stable gold cores were activated to the radioactive isotope Au-198 with an activity of 1 MBq for calibration-validation purposes and 27.5 MBq for experimentation purpose. Au-198 has been widely considered as a preferred tracer isotope in RPT experimentation since it emits relatively low-energy photons with an energy of 412 keV and has a short half-life time of approximately 2.7 days (Roy et al., 2002).

$$^{197}_{79}\mathrm{Au} + ^{1}_{0} \longrightarrow \mathrm{n}^{198}_{79}\mathrm{Au} \underset{\gamma,\beta^-}{\longrightarrow} ^{198}_{80}\mathrm{Hg}$$

At early stages in the design of RPT experiments radiation safety should be considered. The tracer particle activity should be carefully considered based on the conditions and requirements of the experiment at hand, and a high activity should only be used if it can be justified. It is for this reason that a 1 MBq tracer particle is used for the static calibration and low-velocity validation measurements. The 1 MBq tracer particle activity was carefully considered to minimize the radiation dose rate for the operators during the experiments. For the reactor experiments the tracer particle with an activity of 27.5 MBq is required to reconstruct the trajectory with a sufficiently high sampling frequency, and therefore justified. To guarantee a safe working environment and minimize the operator radiation dose, the setup was controlled from a workstation outside the setup room.

2.2. Reconstruction of tracer particle position

When a γ-radiation emitting tracer particle is positioned within the FOV, radiation passing through the slit collimators hits the scintillation crystals, as schematically depicted in Fig. 1.1. Each photon that hits one of the scintillation crystals is absorbed and re-emitted within the visible light spectrum. Subsequently, a photodiode converts the re-emitted light into an electrical current corresponding to the energy of the incident photon. The energy of the

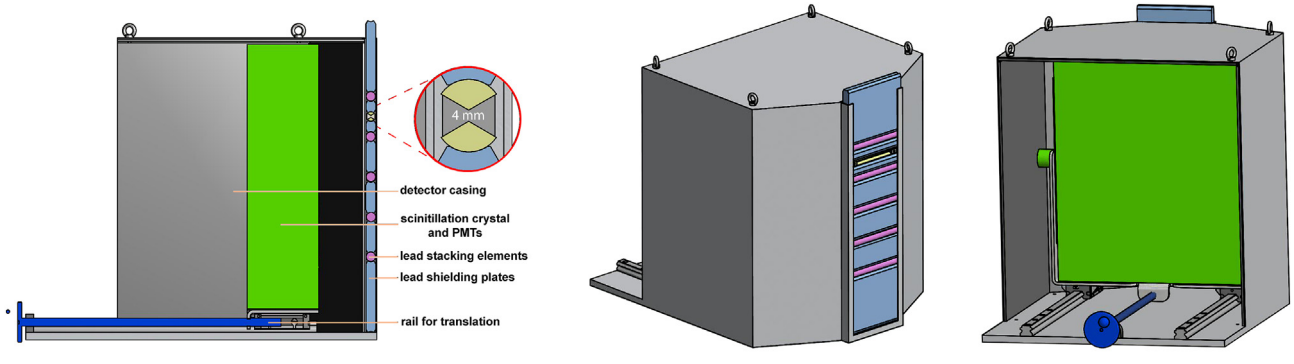

(a) Side view (b) Orthographic view (c) Back view

Fig. 2. Schematic representation of a detector. The gray color represents the detector casing, the blue-gray color the lead shielding plates, the purple color the lead plate stacking elements, the green color the scintillation crystal and photomultiplier tubes, and the dark blue color a rail to translate the scintillation crystal. The 4 mm slit collimator is indicated in sub-figure (a).

incident photon can be determined from the amplitude of the electrical signal. The coordinates of the incident photon hit are determined from the distribution of the signals coming from the PMTs. The data acquired with the detectors is processed by an in-house LabVIEW program, which produces a list containing the xz-coordinates of the activated pixels of each detector, the photon energies, and times of detection.

The coordinates of all photon hits detected by a scintillation crystal can be combined to create a two-dimensional projection of the incoming radiation consisting of 512 × 512 pixels with a pixel size of 1.072 mm. To reconstruct the position of the radioactive tracer particle from its projections on the three detectors, a backward projection method is employed. The workflow for reconstructing the tracer particle position from the detector output data is schematically depicted in Fig. 3.

First, the raw data is sorted for the detector where the photon hit was detected. Then, an energy filter is applied to remove hits originating from the background and scatter radiation. The energy filter bandwidth is determined by taking into consideration the characteristic photon energy of the tracer isotope that is used in the experiments. In this work, an energy filter bandwidth of 400–600 keV is used. Next, the reconstruction sampling frequency is selected, i.e. the number of reconstructions performed per second. The maximum sampling frequency achievable for reconstruction is directly related to the count rate detected by the detector, which in turn is a function of the source activity and distance to the detector (Mostoufi et al., 2003). Due to the slit collimator detector configuration, the projection of the tracer particle on each scintillation crystal appears as a horizontal line at a specific height. Only the height of the projected line is required to reconstruct the tracer particle position, and therefore the two-dimensional detector image is reduced to a one-dimensional image. For each frame, the number of detected photons is counted at each detector z-coordinate pixel value. An example of a histogram of detected photons originating from a static tracer particle is plotted in Fig. 4. The detector configuration and stochastic nature of radiation result in a Poisson distribution. The Poisson distribution can be approximated with a Gaussian model for sufficiently large

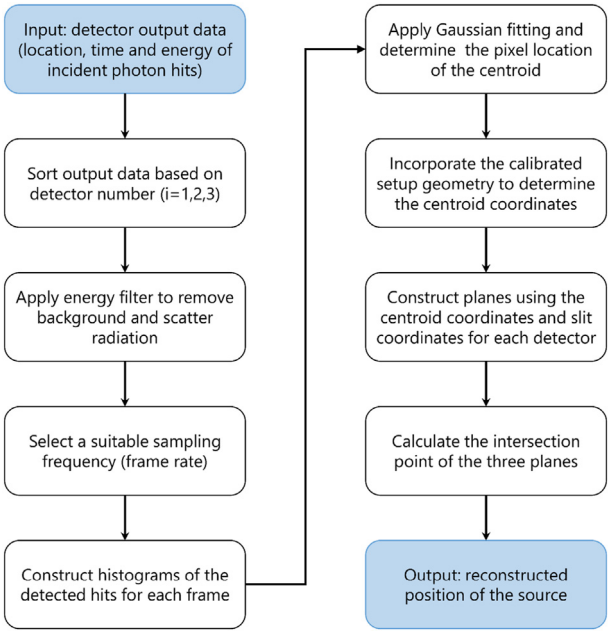

Fig. 3. The reconstruction data processing workflow: from detector output data to the reconstructed position.

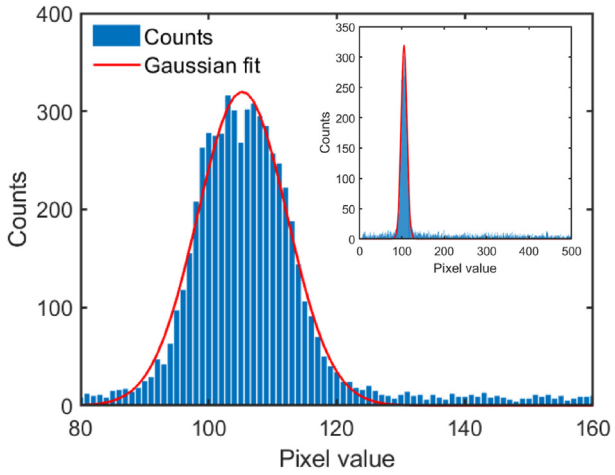

Fig. 4. The distribution of detected photons and corresponding Gaussian fit for a static grid point. The Gaussian fit centroid pixel value is used as input in the reconstruction algorithm.

data sets. Therefore, a Gaussian model is fitted to the distribution, represented by the red line in Fig. 4. The centroid of the Gaussian fit best represents the height of the line projection, and therefore, the pixel value of the centroid is utilized in the position reconstruction.

To incorporate the output from the three detectors, a geometric origin is defined as the midpoint of the FOV. The locations of the scintillation crystals and slit collimators relative to the origin are calculated. For each detector (i = 1, 2, 3) a plane is reconstructed using a set of three points indicated in Fig. 5(a): P_i represents the Gaussian fit centroid pixel value in the center of the detector, while L_i and R_i correspond to the middle points on the left and right side of the slit, respectively. By constructing a plane through these points for all three detectors simultaneously, a unique intersection point is formed. The coordinates of this intersection point represent the reconstructed position of the radioactive tracer particle, as shown in Fig. 5b. Each set of points, $\mathbf{P}_i$, $\mathbf{L}_i$, and $\mathbf{R}_i$ results in the plane equation:

$$d_i = \mathbf{n}_i \cdot \mathbf{x} \tag{1}$$

where $\mathbf{x}$ is the general xyz-position vector.

$$\mathbf{a}_i = \mathbf{L}_i - \mathbf{R}_i \tag{2}$$

$$\mathbf{b}_i = \mathbf{L}_i - \mathbf{P}_i \tag{3}$$

$$\mathbf{n}_i = \mathbf{a}_i \times \mathbf{b}_i \tag{4}$$

$$d_i = \mathbf{L}_i \cdot \mathbf{n}_i \tag{5}$$

The system of equations can be written in matrix representation which provides a straightforward manner of solving for the plane intersection point $\dot{x}$

$$\mathbf{N}\dot{\mathbf{x}} = \mathbf{D} \tag{6}$$

$$\begin{pmatrix} \mathbf{n_1}^T \\ \mathbf{n_2}^T \\ \mathbf{n_3}^T \end{pmatrix} \begin{pmatrix} \dot{x} \\ \dot{y} \\ \dot{z} \end{pmatrix} = \begin{pmatrix} d_1 \\ d_2 \\ d_3 \end{pmatrix} \tag{7}$$

The intersection point of the planes, i.e. the reconstructed position of the tracer particle, is then computed from

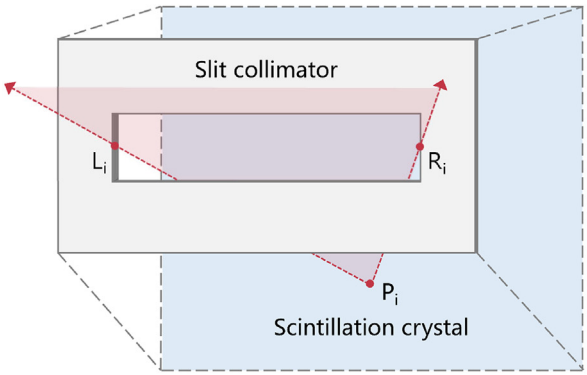

(a) The points used to construct a plane: (1) location of the hit on the detector; (2) left side; and (3) right side of the slit.

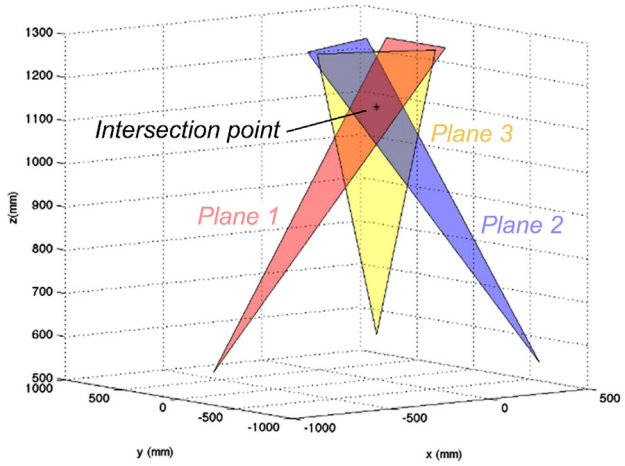

(b) Intersection point of the planes constructed from the three detectors.

Fig. 5. The tracer particle position is reconstructed by constructing a plane from each detector and computing the unique intersection point of these planes.

$$\dot{\mathbf{x}} = \mathbf{N}^{-1}\mathbf{D} \tag{8}$$

2.3. Setup calibration

The coordinates of the reconstructed position are calculated using System of Equation (7). However, these calculations can be affected by potential inaccuracies in the hand-measured positions of $\mathbf{L}_i$ and $\mathbf{R}_i$. To ensure reconstruction with high spatial accuracy and precision, calibration of the RPT setup geometry is required. The calibration process aims to correct for errors in the spatial geometry of the setup caused by manual measurements. This is achieved by minimizing the sum of the squares of the residuals for a large number of true tracer particle positions and the corresponding reconstructed tracer particle positions, using a constrained non-linear least-squares optimization algorithm in MATLAB. The calibration workflow is illustrated in Fig. 6.

A three-dimensional cylindrical grid of 95 predefined tracer particle positions and reconstructed positions was constructed. For this purpose, a 300 mm circular solid aluminum optical breadboard with holes spaced 25 mm apart on the diagonal was mounted on a rotation table, which was then mounted on a lifting table. The 1 MBq Au-198 tracer particle (see Section 2.1) was placed in a plastic shielding and mounted on top of a 300 mm aluminum bar with a screw thread, as shown in Fig. 7.

The cylindrical grid was constructed by incrementally translating the tracer particle in the xy and xz-planes and successively rotating the tracer particle in the xy-plane. The coordinates of the known tracer particle positions are denoted as the true positions. At each grid position, the emitted γ-radiation was detected for a duration of 21 s to allow accurate Gaussian fitting and centroid determination. The position was reconstructed using the workflow described in Section 2.2. A selection of 35 true and reconstructed positions was used as input for the optimization algorithm. As described later in Section 2.4, the full grid consisting of all the true positions and reconstructed positions was used for the validation of the method.

Finally, an initial guess of the hand-measured setup geometry is required. The geometry is described by six (x,y,z) coordinates, representing the left and right sides of the slit collimators (see Fig. 5(a)), as well as three (x,y) coordinates corresponding to the middle points of the detectors. A constrained non-linear least squares optimization method in MATLAB is used to minimize the sum of the squares of the residuals by varying the hand-measured geometry parameters with upper and lower bound values of 50 mm. The output of the algorithm is a calibrated set of geometry values, encompassing the spatial orientation of the detectors. These calibrated geometry values substitute the initial guess hand-measured values and are utilized in subsequent processing steps.

2.4. Method validation

The performance of the setup is validated using both static and dynamic experiments, utilizing the calibrated geometry. The validation process consists of two parts. Firstly, the spatial accuracy and precision of the calibrated setup are assessed under static conditions using the complete cylindrical grid. As outlined in Section 2.3, the grid comprises 95 positions distributed within a volume of 75 mm radius and 200 mm height. For each grid point, the absolute error between the coordinates of the true position and the reconstructed position is calculated, allowing evaluation of the spatial accuracy and precision of the reconstruction.

Secondly, dynamic validation experiments are conducted. Employing the same experimental setup as the static validation experiments (see Fig. 7), the tracer particle is horizontally rotated at varying radii and angular velocities while maintaining a fixed height in the middle of the FOV. The acquired data from both static and dynamic validation experiments is processed at different reconstruction sampling frequencies to examine the relationship between spatial precision and sampling frequency.

3. Results and discussion

3.1. Non-calibrated reconstruction

To emphasize the importance of calibrating the RPT setup geometry, reconstruction of the grid positions (see 2.3) was performed using the hand-measured geometry. The reconstruction processing workflow was applied, with the hand-measured geometry as input, to reconstruct the tracer particle positions. The true positions and the reconstructed positions before calibration are plotted in Fig. 8(a).

It can be observed that the reconstructed positions (in blue) deviate significantly from the true positions (in red). Notably, the spatial error becomes more pronounced for lower z-coordinate values. During the reconstruction, the intersection point of three planes originating from the three detectors is determined. The

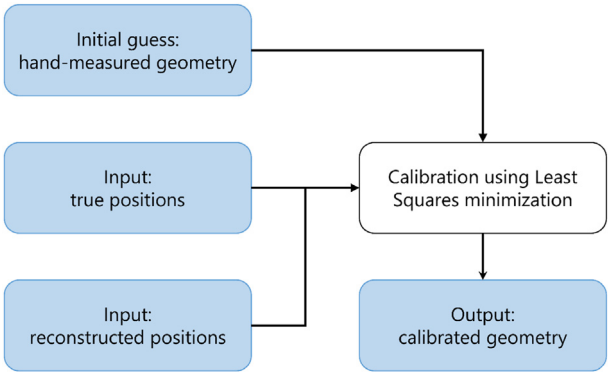

Fig. 6. The calibration processing workflow. Calibration requires an initial guess geometry and true and reconstructed tracer particle locations as input. The algorithm returns a calibrated geometry.

spatial error becomes infinitely large if the three planes are parallel to each other. When the planes are nearly parallel, as is the case for z-coordinate values close to the slit height, even slight deviations in the plane angles result in substantial variations in the coordinates of the intersection point. Consequently, the reconstruction exhibits poor spatial accuracy and precision for lower z-coordinate positions. The spatial error, represented by the absolute distance between the true grid point and the corresponding reconstructed grid point, is illustrated for the x, y, and z coordinates in Fig. 8(b). It can be observed that the mean average errors (MAE) are 17.09, 21.88, and 3.90 mm for the x, y, and z-coordinate, respectively. Moreover, the standard deviations (σ) are 4.21, 4.68, and 1.88 mm for the x, y, and z-coordinate, respectively. The cumulative percentage curve shows that 90 percent of the grid points have a spatial error smaller than 24 mm, 26 mm, and 6 mm in x, y, and z, respectively. The MAE and standard deviation in x and y exceed the acceptable range for the desired particle tracking applications in lab-scale systems. Thus, reconstruction of the tracer particle position using the hand-measured setup geometry does not yield satisfactory spatial accuracy and precision.

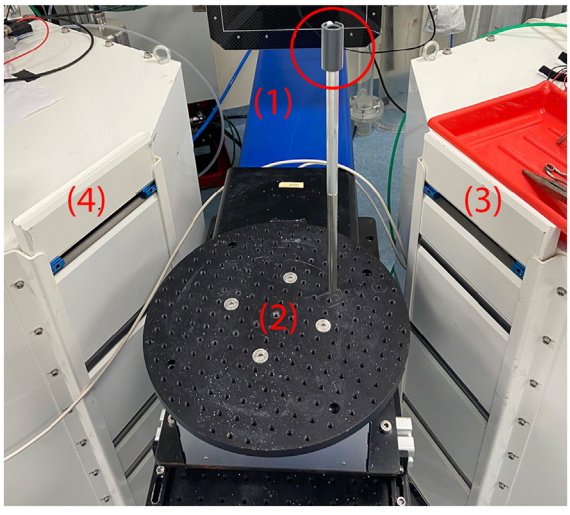

Fig. 7. The experimental calibration setup: 1) plastic container containing the tracer particle; 2) rotation table; 3) slit of detector 1 and; 4) slit of detector 3.

3.2. Setup calibration

To improve the spatial accuracy and precision of the reconstruction, a calibration workflow was implemented as detailed in Section 2.3. By minimizing the absolute error between the true position and the reconstructed position for the selected 35 grid points, the constrained optimization algorithm returns calibrated geometry values. The hand-measured and calibrated spatial orientation of the three detectors is illustrated in Fig. 2.1. It can be observed that the optimization algorithm yields a geometry in which each detector undergoes slight translation and rotation relative to its orientation in the hand-measured geometry, effectively correcting for measurement inaccuracies.

3.3. Method validation

3.3.1. Static validation

In the implemented method, the calibrated geometry is utilized for the reconstruction of the tracer particle positions. As explained in Section 2.4, the tracer particle was positioned at 95 known locations to validate the static reconstruction. The true positions and the reconstructed positions after calibration are depicted in Fig. 9(a). It can be observed that for a large number of the grid points the reconstructed positions (in blue) overlap with the true positions (in red), which is in sharp contrast to the reconstruction before calibration (Fig. 8(a)), in which the positions deviate significantly. This qualitative observation demonstrates substantial improvement in spatial accuracy achieved through calibration.

To assess the spatial accuracy quantitatively, the absolute spatial error between the reconstructed position and the true position is presented for the x, y, and z-coordinate in Fig. 9(b). It can be observed that the mean average errors (MAE) are significantly reduced to 0.87, 0.62, and 0.87 mm for the x, y, and z-coordinate, respectively. Consequently, calibration has reduced the MAE by a factor of 20, 35, and 4 in x, y, and z, respectively, compared to the reconstruction before calibration. Similarly, the standard deviations (σ) after calibration are reduced to 1.09, 0.61 and 0.55 mm for the x, y and z-coordinate, respectively. This demonstrates that calibration improves both the spatial accuracy and the spatial precision of the reconstruction. The cumulative percentage curve shows that 90 percent of the grid points exhibit a spatial error smaller than 1.5 mm in x and z, and smaller than 1.3 mm in y. Fig. 9(b) also illustrates that lower z-coordinate grid points are associated with higher spatial errors in x and y, similar to the reconstruction before calibration. Therefore the desired volume of interest must be placed above the detector slits. Yet, the calibration yields satisfactory spatial accuracy and precision.

The aforementioned reconstruction process involves determining the tracer particle position based on the counts acquired over a sampling time of 21 s. Consequently, the sampling frequency of this reconstruction is approximately 0.05 frames per second (fps). In this case, all the counts detected during the measurement time window are collectively utilized to calculate a single reconstructed position. However, since many applications involve dynamic scenarios, it is desirable to increase the sampling frequency to be able to reconstruct the trajectory of a dynamic tracer particle with sufficient accuracy and precision. Thus, the entire grid is reconstructed at sampling frequencies of 0.125 fps, 0.5 fps, 2 fps, and 4 fps. Fig. 10 presents a two-dimensional top-view of the full grid, showcasing the true positions (in red) and the reconstructed positions (in blue) for the different sampling frequencies.

It can be observed that the sampling frequency has a significant impact on the spatial precision of the reconstruction. When the sampling frequency increases from 0.05 fps to 0.125 fps, the 285 reconstructed positions (3 for each of the 95 grid points) are closely

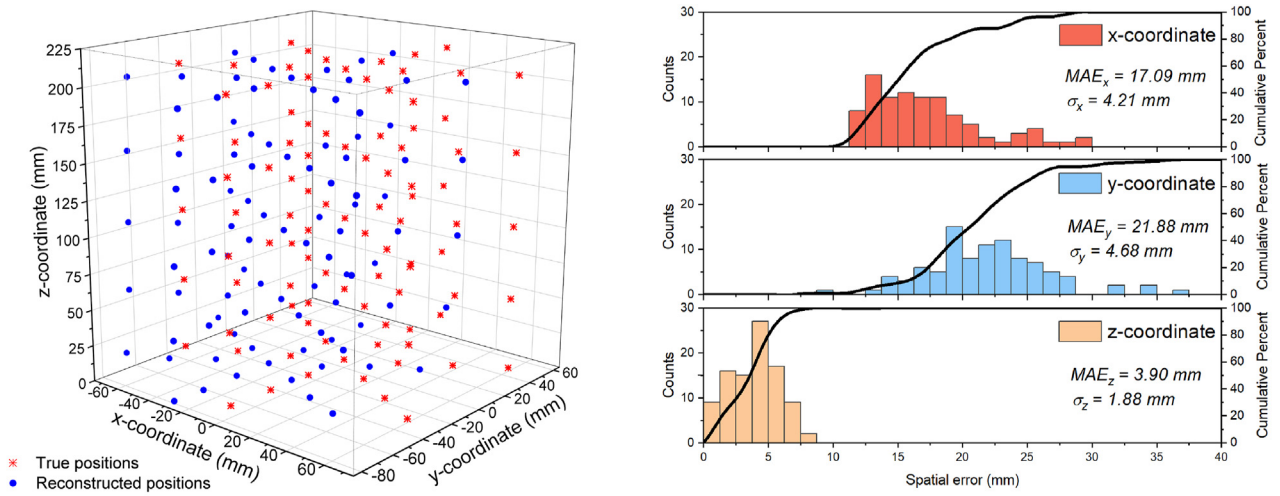

(a) Three-dimensional scatter of the true grid positions and reconstructed grid positions before calibration.

(b) Absolute spatial error of the true position relative to the reconstructed position before calibration.

Fig. 8. Reconstruction of the 95 grid positions before calibration.

clustered around their respective true positions, resulting in a low MAE (1.45 mm) and standard deviation (1.45 mm). This demonstrates that a high level of spatial precision is achieved. However, as the sampling frequency further increases to 0.5 fps, 2 fps, and 4 fps, the number of reconstructed positions increases, while the spatial precision decreases. This results in the reconstructed positions being loosely scattered around the true positions, leading to a higher MAE and standard deviation. The decrease in spatial precision is attributed to the reduction in the number of counts (i.e., detected γ-ray photons) available for each frame during the reconstruction. With a higher sampling frequency, the same number of counts is now distributed over a larger number of successive frames, leading to the availability of fewer counts per frame. Consequently, the Gaussian model is fitted to a smaller data set, negatively influencing the accuracy of the fit. This effect is observable by comparing the reconstruction of a single grid point for a sampling frequency of 0.125 fps and 2 fps, as depicted in Fig. 11.

At a sampling frequency of 0.125 fps, the large number of counts allows that the Poisson distribution can be approximated accurately with a Gaussian model. In contrast, when the sampling frequency is increased to 2 fps, the underlying distribution is poorly sampled, resulting in a Gaussian fit with reduced confidence. Mostoufi et al. (Mostoufi et al., 2003) showed that the number of recorded incident photon hits is directly proportional to the sampling time of the reconstruction. Furthermore, they demonstrated that the spatial precision is inversely proportional to the square root of the sampling time. The same fundamental relationship between the spatial precision and reconstruction sampling time is observed here by comparing the standard deviation for the sampling frequencies of 0.125 fps and 0.5 fps.

As the sampling frequency is further increased, the number of counts in some segments becomes insufficient for reliable Gaussian fitting and reconstruction of the tracer particle's position. This phenomenon is evident when comparing the reconstructions at 2 fps and 4 fps in Fig. 10. Increasing the sampling frequency by a factor of two should also lead to a proportional increase in the number of reconstructed positions. However, as can be observed, the number of reconstructed positions only increases by 10%, indicating that a large number of attempted reconstructions do not result in a reconstructed position due to unsuccessful Gaussian fitting. Interestingly, the standard deviation of the error decreases from 7.89 mm to 5.64 mm. This is attributed to the large number of failed reconstructions at a sampling frequency of 4 fps. The frames that have an extremely low number of counts at a sampling frequency of 2 fps result in a reconstructed position with poor spatial precision, essentially becoming an outlier in the data set. When trying to reconstruct these positions at an even higher sampling frequency, they can no longer be reconstructed, resulting in the outliers being discarded from the data set and thereby improving the overall spatial precision. Notably, further increasing the sampling frequency would result in a further decrease in the number of reconstructed positions, which is highly undesirable if one would like to reconstruct the trajectory of a moving tracer particle.

However, the above is not necessarily a limitation of the RPT method. As described earlier, the spatial precision is inversely proportional to the square root of the sampling time. To improve the spatial precision, or conversely the sampling frequency, with a factor of 2, an increase in the number of detected incident photons with a factor of 4 is required. As the number of detected photons is directly proportional to the source's activity, improved precision can be accomplished by increasing the activity of the tracer particle. This can be achieved by either increasing the mass of the radionuclide or extending the activation time of the tracer.

3.3.2. Dynamic validation

The aforementioned reconstructions focused on a static tracer particle. However, since most applications are dynamic, it is crucial to validate the technique's performance in reconstructing the trajectory of a moving tracer particle. Therefore, a series of dynamic experiments were conducted in which the 1 MBq tracer particle was horizontally rotated at radii of 25, 50, and 75 mm, with angular velocities of 5 and 10° per second. The true trajectories and the corresponding reconstructed trajectories are presented in Fig. 12 for the different radii and angular velocities.

The true trajectory of the tracer particle is represented by a red circle, while the reconstructed positions are depicted as blue scatter dots in Fig. 12. To evaluate the spatial precision of the reconstruction, the reconstructed positions were fitted to a circle, indicated by the blue circles in the figure, with their corresponding radii displayed. The close alignment between the true trajectory and the reconstructed trajectory indicates a high level of spatial precision. No instances of poorly reconstructed positions were observed

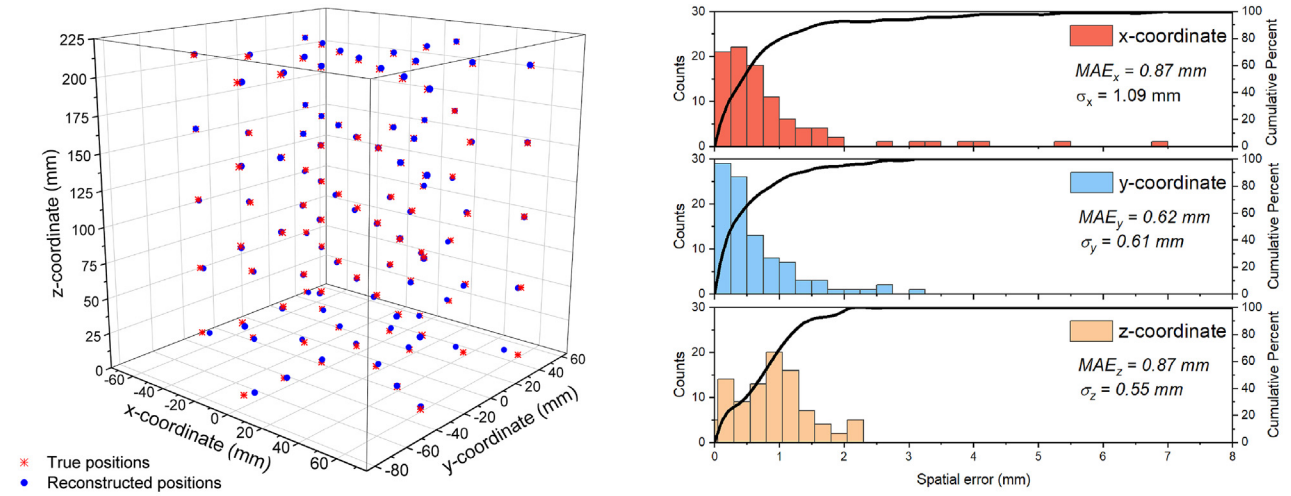

(a) Three-dimensional scatter of the true grid positions and reconstructed grid positions after calibration.

(b) Absolute spatial error of the true position relative to the reconstructed position after calibration.

Fig. 9. Reconstruction of the 95 grid positions after calibration.

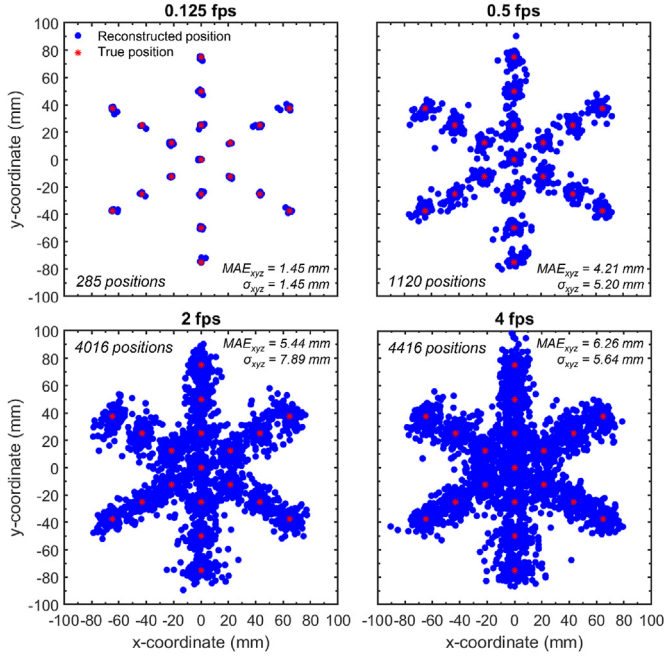

Fig. 10. Reconstruction of true positions and reconstructed positions of the 1 MBq tracer particle with a sampling frequency of 0.125, 0.5, 2, and 4 fps. The number of reconstructed positions, Pythagorean mean absolute error (MAE_{xyz}) and standard deviation σ_{xyz} are indicated in each sub-figure.

across all cases. To quantify the spatial precision, the absolute percentage errors between the true radii and the fitted radii were computed. The error values range from 0.03% (R = 75 mm, $\omega = 5°$ per second) to 0.52% (R = 25 mm, $\omega = 5°$ per second), emphasizing reconstruction with excellent spatial precision. Moreover, from the temporal evolution of the y-coordinate, it can be observed that the reconstruction correctly captures the trajectory in time.

During the reconstruction time window, the movement of the tracer particle introduces a spread of radiation over a larger area of the detector, resulting in a Gaussian fit with a lower peak and increased Full Width Half Maximum (FWHM). This phenomenon shares similarities with motion blur observed in optical cameras. Consequently, the reconstructed position of a moving tracer particle represents an average position rather than an instantaneous one. Fig. 13 depicts the obtained distribution of counts and the corresponding Gaussian fit for a relatively low and high linear velocity.

When comparing the two cases, it can be observed that the count distribution is narrower (FWHM = 13 px) and exhibits a higher peak when the linear velocity is low, which is the case for a small radius (25 mm) and low angular velocity (5° per second). Conversely, when the linear velocity is increased, as in the case of a large radius (75 mm) and high angular velocity (10° per second), the particle covers a greater distance within a single reconstruction frame. This leads to a broader distribution of the counts (FWHM = 20 px) with a lower peak. Yet, as demonstrated in Fig. 12, the reconstruction accurately captures the tracer particle trajectory with sufficient spatial precision in both scenarios.

The horizontal rotation trajectory of the 1 MBq tracer particle at a radius of 50 mm and angular velocity of 5° per second was reconstructed with a sampling frequency of 0.125, 0.5, 2 and 4 fps to examine the impact of the sampling frequency on the spatial precision under dynamic conditions. Fig. 14 displays the reconstructed trajectories for each sampling frequency.

From the figure, it can be observed that the true trajectory closely follows the reconstructed trajectory (in red) at sampling frequencies of 0.125 and 0.5 fps, indicating high spatial precision. However, at a sampling frequency of 2 fps, the reconstructed positions scatter more loosely around the true trajectory, suggesting reduced spatial precision compared to the low sampling frequencies. Despite the random scattering around the true trajectory, the fit remains accurate, with a spatial absolute percentage error of only 0.02% relative to the true radius. This demonstrates that the trajectory can still be accurately reconstructed even at the reduced sampling frequency. However, further increasing the sampling frequency to 8 fps results in the inability to accurately reconstruct the tracer particle's trajectory. This is indicated by the poor spatial precision and the decrease in the number of reconstructed positions. Similar to the reconstruction of the static tracer particle at 4 fps, a larger number of frames contain too few counts to perform Gaussian fitting and reconstruct the tracer particle's position. As described earlier, it should be noted that increasing

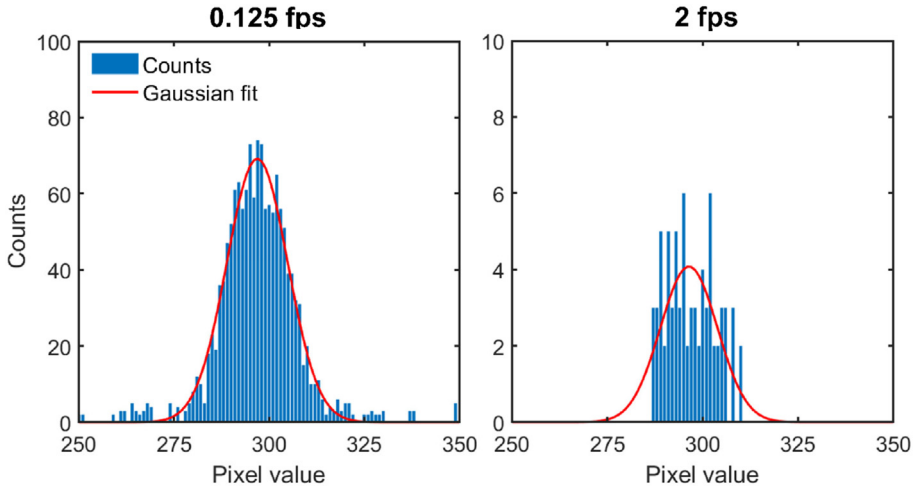

Fig. 11. Example of the histogram and Gaussian fit for a single grid point reconstructed with a sampling frequency of 0.125 fps (left) and 2 fps (right).

the activity of the tracer particle would lead to trajectory reconstruction with improved spatial precision at high sampling frequencies.

4. Case study: Flow field evaluation in a lab-scale horizontal stirred bed reactor

4.1. Setup description

Through static and dynamic validation, the presented RPT method has been demonstrated to be able to reconstruct the three-dimensional position of a tracer particle with high spatial accuracy and precision. To showcase the technique's applicability in characterizing hydrodynamics in multi-phase systems, a hydrodynamic study was conducted using a 27.5 MBq radioactive tracer particle within a lab-scale horizontal stirred bed reactor (HSBR). HSBRs play an important role in the processing of granular materials and find applications in various fields, such as biomass pyrolysis (Xi et al., 2015) and polyolefin manufacturing (Caracotsios, 1992; Dittrich & Mutsers, 2007). The HSBR generally contains a granular bed that is mildly stirred by a series of blades attached to a center shaft, resulting in a well-mixed system.

In this work, a laboratory-scale HSBR was developed to investigate the hydrodynamics in non-reactive environments, aiming to enhance the understanding of granular motion in HSBRs in polypropylene manufacturing applications. The HSBR, presented in Fig. 15, consists of a 140 mm outer-diameter cylinder with a length of 150 mm. The cylinder incorporates an agitator comprising a

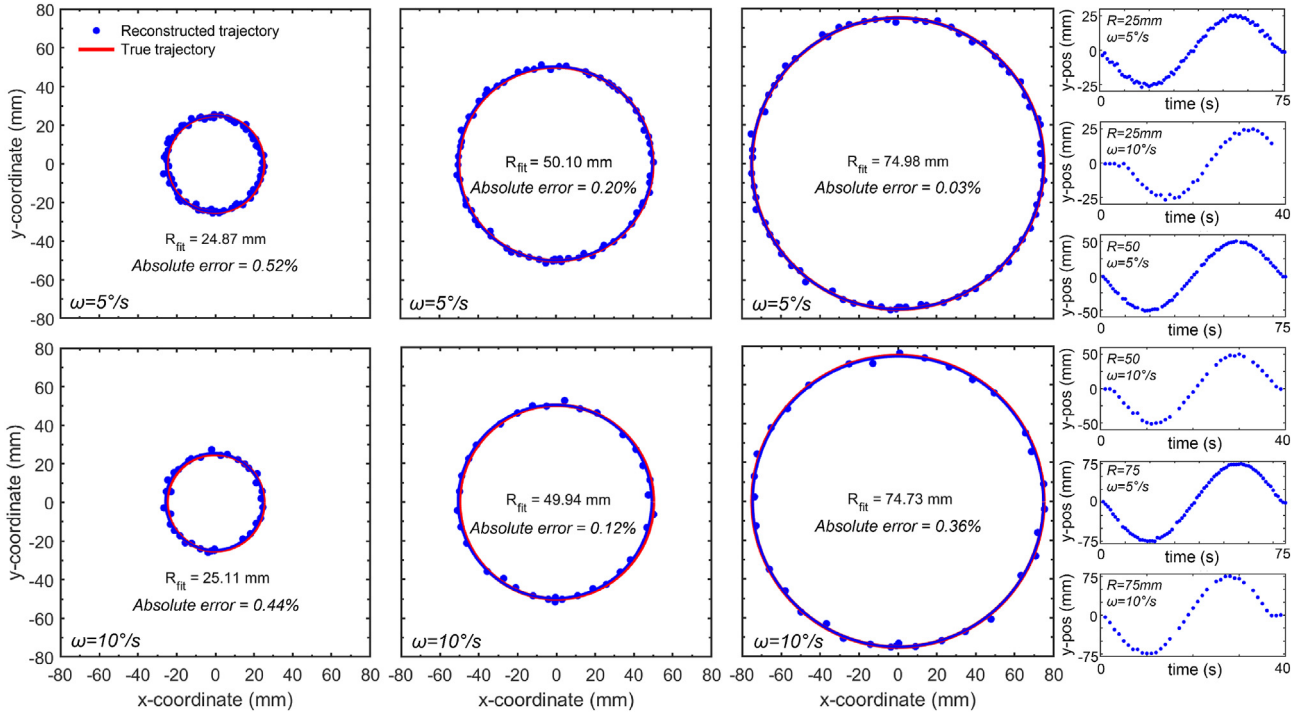

Fig. 12. Reconstruction of the true and reconstructed trajectory for horizontal rotation at 25, 50 and 75 mm radii and angular velocity of 5° and 10° per second with a sampling frequency of 1 fps. At the right, the temporal evolution of the y-position is shown for one rotation for each measurement.

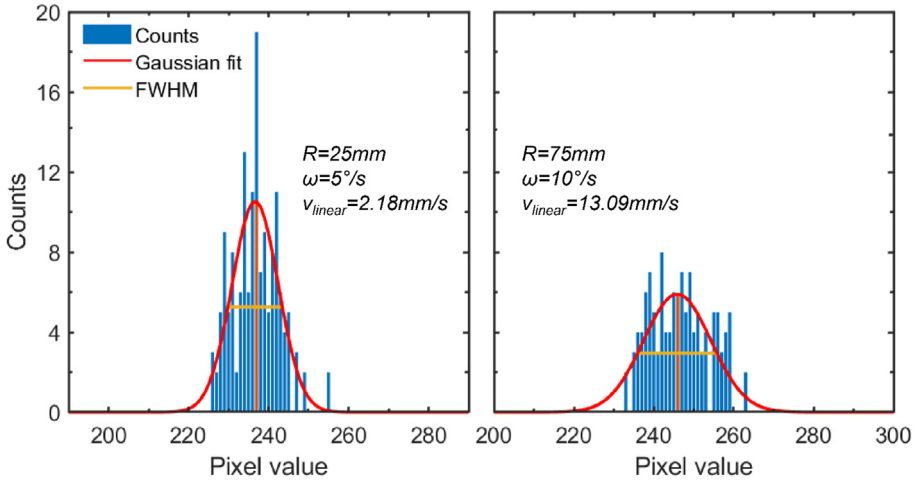

Fig. 13. Influence of linear velocity on the distribution of counts and Gaussian fit for the horizontal rotation experiments with a 1 MBq tracer particle. Reconstruction is performed with a sampling frequency of 1 fps.

central shaft with seven blade positions. Each position is equipped with two blades, with each blade positioned 90° apart from its neighboring blades. Both the cylinder and the agitator are constructed from polycarbonate to reduce attenuation during the experiments.

4.2. Radioactive particle tracking experiments

To conduct RPT experiments, the RPT setup was first calibrated following the workflow outlined in Section 2.3. Subsequently, the HSBR was positioned in the center of the FOV of the RPT setup. A mass of 410 g industrial-grade polypropylene reactor powder, with

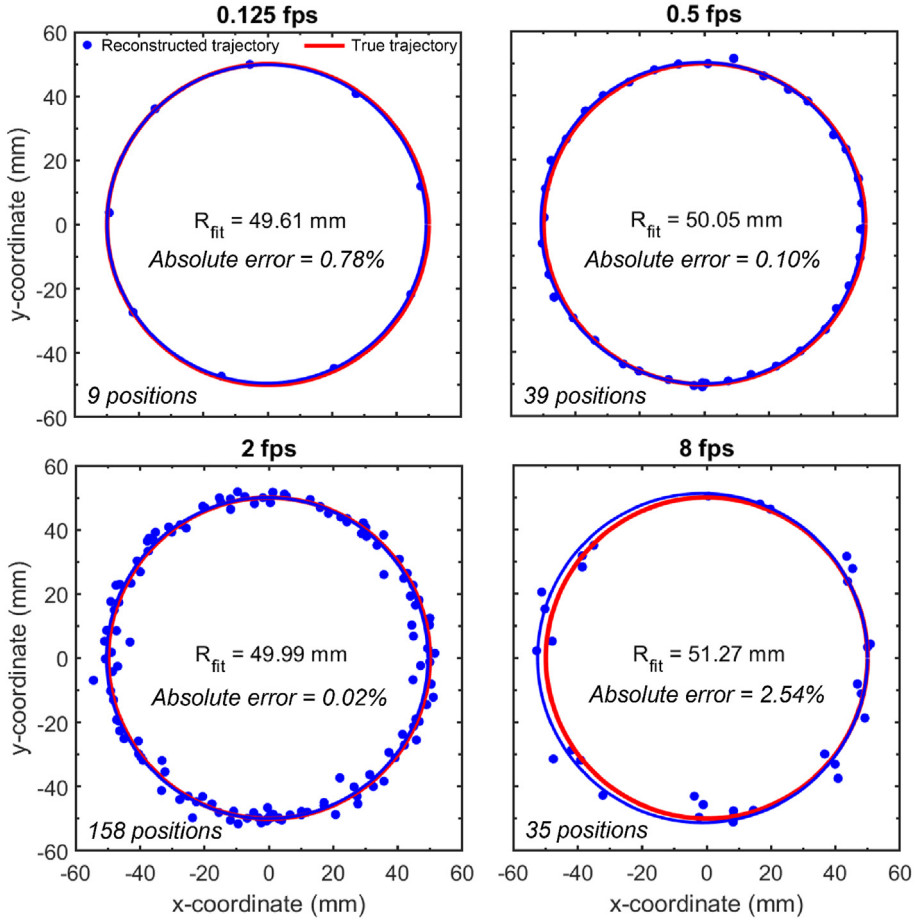

Fig. 14. Reconstruction of the true and reconstructed trajectory for horizontal rotation at 50 mm radius and angular velocity of 5° per second, reconstructed with a sampling frequency of 0.125, 0.5, 2 and 4 fps.

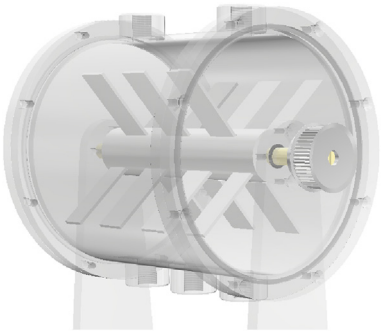

Fig. 15. Schematic representation of the laboratory-scale horizontal stirred bed reactor used in the case study.

a bulk density of $\rho_b = 368$ kg m^{-3} and a median diameter of $D_{v,50} = 985$ µm, was loaded into the reactor, resulting in a 60% volume fill grade. The 27.5 MBq Au-198 radioactive tracer particle, composed of 1.6 mg Au-198 embedded in a 1.8 mm polystyrene bead with an air gap (see Section 2.1), was added to the HSBR. The agitator was then rotated at a rotation speed of 20 rpm using an electric motor with a belt drive. The tracer particle's trajectory was recorded for a duration of 10 min, equivalent to 200 impeller rotations. To ensure a safe working environment and minimize radiation exposure to the operators, the experimental procedure was controlled from a workstation situated outside the setup room. The three-dimensional trajectory was reconstructed based on the workflow described in Section 2.2. The reconstruction was performed with a sampling frequency of 10 fps, i.e. a sampling time of 100 ms.

4.3. Results and discussion

Fig. 16 displays the time-resolved trajectory for a 1 min time interval, providing 0°, 45°, and 90° angle views to illustrate the three-dimensional nature of the reconstruction. Each blue scatter marker represents a unique reconstructed position accumulated during the 1 min time interval. The 90° angle view exhibits three consecutive reconstructed positions: the instantaneous reference position, the reference position after 100 ms, and the reference position after 200 ms. The small spatial step observed between these consecutive reconstructed positions shows that a sampling frequency of 10 fps is sufficient to track the trajectory of the tracer particle within the HSBR when operated at a rotation speed of 20 rpm.

The time-averaged flow behavior of the tracer particle can be characterized from the acquired positions data set. Fig. 17 shows the particle positions in the xz-plane accumulated during the 10-min measurement time, allowing visualization of the particle circumferential and radial motion. Since the agitator rotates in a clockwise direction, the granular bed undergoes clockwise mixing,

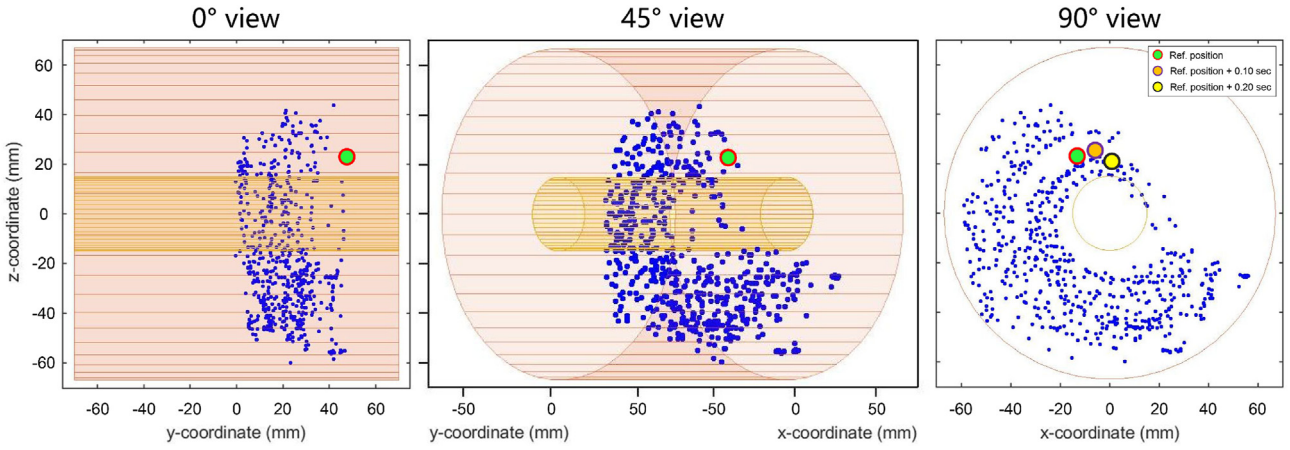

Fig. 16. Reconstructed positions of the tracer particle in the HSBR accumulated for a time period of 1 min. The instantaneous position is referenced by the red-outlined green dot. Two consecutive reconstructed positions are indicated in the 90° view. The reactor wall and stirrer shaft are indicated with a red and yellow color, respectively.

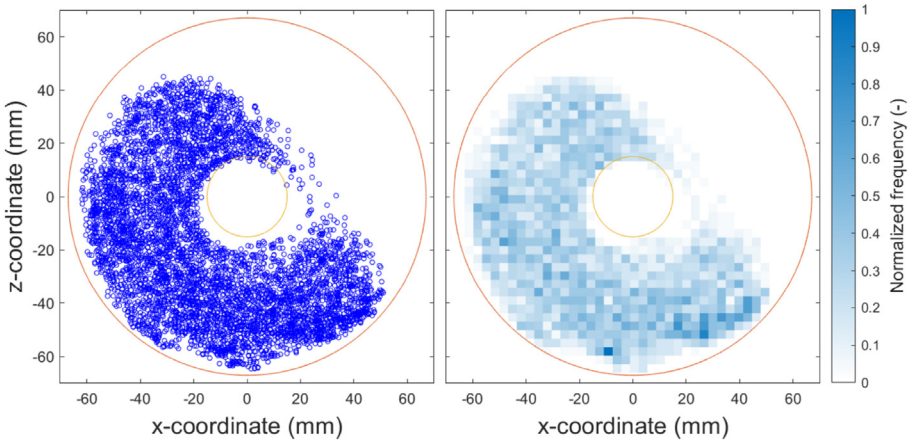

Fig. 17. Reconstructed spatial distribution (left) and normalized spatial frequency distribution (right) measured for a time period of 10 min shown for the x-z plane.

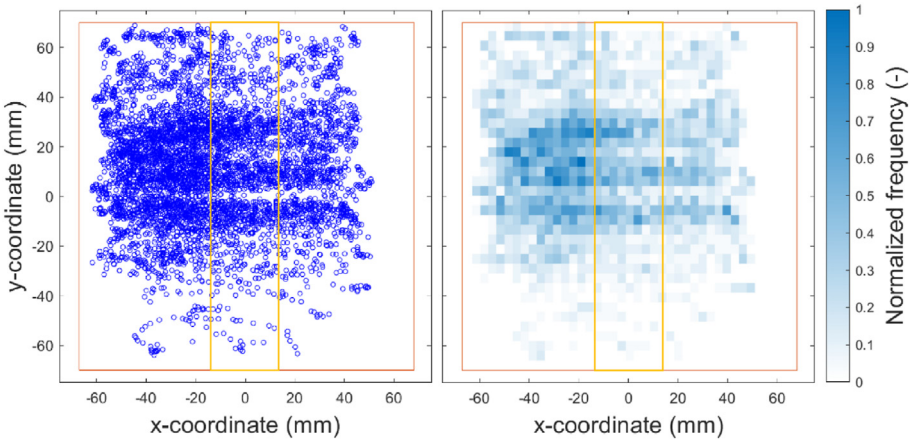

Fig. 18. Reconstructed spatial distribution (left) and normalized spatial frequency distribution (right) measured for a time period of 10 min shown for the x-y plane.

causing the left side of the bed to move upward and flow freely over the shaft. From the scatter plot, Fig. 17-left, it can be observed that the tracer particle exhibits good radial dispersion throughout the bed. During the 10-min measurement, the particle follows clockwise trajectories near the reactor wall, through the center of the granular bed, and close to the shaft. This is an important observation, as any tracer particle used to evaluate flow behavior in a particular medium should exhibit similar dynamics to the medium itself. A mesh-grid function in MATLAB was used to compute the normalized frequency, representing the solids hold-up, for a rectangular grid of the HSBR xz-plane. The solids hold-up map, depicted in Fig. 17-right, reveals the absence of dead zones, which would be indicated by dark blue coloration, and demonstrates a uniform radial solids hold-up throughout the bed.

Fig. 18 depicts the particle positions in the xy-plane accumulated during the 10-min measurement time, providing insight into the axial motion of the tracer within the reactor. It can be observed from the scatter plot, depicted in Fig. 18-left, that the tracer particle exhibits significant axial movement throughout the HSBR, with reconstructed positions at nearly every coordinate value along the y-axis during the 10-min measurement period. The solids hold-up map, depicted in Fig. 18-right, demonstrates a heterogeneous distribution. From the figure distinct zones with a dark blue coloration (i.e. high solids hold-up) and light blue to white coloration (i.e. low solids hold-up) can be identified.

Finally, the velocity field of the tracer particle is computed from the time-resolved positions using a center-difference approach

$$v_{ij}(t) = \frac{x_i(t_j + \Delta t) - x_i(t_j)}{\Delta t} \tag{9}$$

The velocity vectors, $v(t)$, at their corresponding position, $x(t)$ are plotted in Fig. 19 for a time interval of 3 min. From the velocity field, two distinct regions can be distinguished. On the one hand, a low-velocity region at the bottom and left side of the bed is recognized when the agitator is the driving force for the motion of the bed. On the other hand, a high-velocity region at the top right side of the bed is recognized when the bed flows freely over the shaft and gravity becomes the dominant driving force, resulting in significantly higher velocities.

The significant variation within the velocity flow field is also clear from the computed velocity statistics. Table 1 presents the median, mean, and maximum velocity of the tracer particle, as well as the velocity at the tip of the impeller blades for a rotation speed of 20 RPM. It is interesting to compare the computed tracer velocity statistics to the tip speed. When the HSBR is operated at a rotation

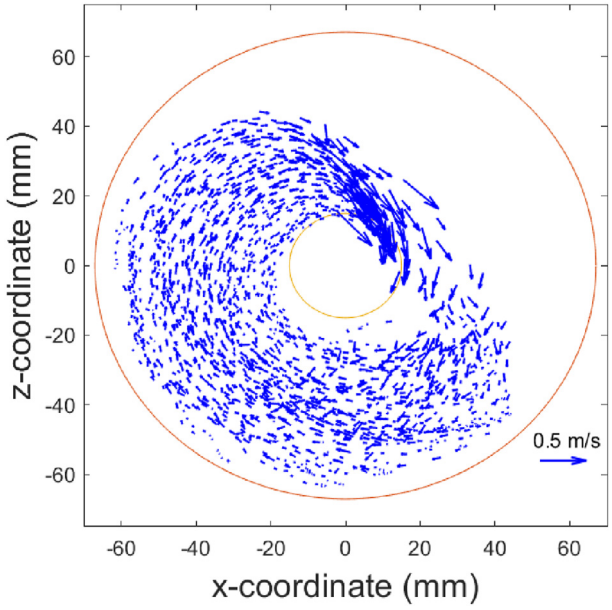

Fig. 19. Reconstructed tracer particle velocity flow field map shown for the x-z plane. The velocity vectors are computed from the time-resolved tracer trajectory measured for a time period of 3 min.

Table 1
Velocity statistics for the velocity quiver plot presented in Fig. 19.

v_{median} (mm/s)	v_{mean} (mm/s)	v_{max} (mm/s)	v_{tip} (mm/s)
60.5	73.6	623.5	140.3

speed of 20 RPM, the mean velocity of the tracer particle is approximately 0.52 times the tip speed. In contrast, the maximum observed velocity is found to be approximately 4.4 times the tip speed. As described above, the high velocity is likely attributed to the gravity experienced by the tracer particle during the flow over the reactor shaft.

The time-resolved tracer particle trajectory, time-averaged solids hold-up profiles, and velocity field, acquired with single-photon emission RPT, can aid in a better understanding of the nature of the flow field in horizontal stirred bed reactors. Moreover, the experimental data sets can contribute to the validation of computational models of the reactors.

5. Conclusions

Radioactive particle tracking is a valuable technique for visualizing flow fields in multi-phase systems, offering potential benefits in process optimization and intensification. However, traditional approaches rely on assumptions in simulating the count rate received by detectors for reconstructing the position of the radioactive tracer particle.

In this paper, we introduced a novel radioactive particle tracking approach based on a fundamentally different reconstruction method. The detected photon hit locations are directly utilized for reconstructing the three-dimensional position of the tracer particle, thereby circumventing the need for assumptions in count rate fluctuations. The setup includes three identical γ-radiation slit collimator detectors positioned equidistantly at 120°. The tracer particle's three-dimensional position is reconstructed by determining the intersection point of three two-dimensional planes originating from the detectors. Through a calibration-experimentation procedure, we achieved a spatial accuracy of approximately 1 mm for tracer particle position reconstruction. In a case study, we demonstrated the application of the method in evaluating the hydrodynamics in a horizontal stirred bed reactor system. The trajectory of a 27.5 MBq tracer particle in the reactor was reconstructed over a 10-min time period with a sampling frequency of 10 fps. Using the reconstructed positions, we analyzed the radial, circumferential, and axial spatial distributions, as well as the velocity flow field. The hydrodynamic insights that can be obtained from radioactive particle experimentation provide valuable information for validating computational models and can contribute to the optimization and intensification of multi-phase flow systems.

Declaration of interests

The authors declare that they have no known competing financial interests or personal relationships that could have appeared to influence the work reported in this paper.

Acknowledgments

The authors would like to express their gratitude to several individuals and organizations for their contributions to this study. They acknowledge Stefan ten Hagen for his involvement in the development of the horizontal stirred bed reactor, Duco Bosma for his contributions to the manufacturing of the tracer particles, and Mehmet Sarilar for performing the neutron activation of the tracer particles. The authors also extend their thanks to the Delft University of Technology Reactor Institute radiation protection service for ensuring a safe working environment during the experiments. Additionally, they acknowledge Kaiqiao Wu for his assistance in data processing.

This work was conducted as part of the "Industrial Dense Granular Flows" project, which received funding from the Dutch Research Council (NWO) through the ENW PPP Fund for the top sectors and from the Ministry of Economic Affairs under the "PPS-Toeslagregeling" framework.

Appendix A

1 γ-radiation detection

The γ-radiation emitted by the tracer particle passes through the slit collimator and reaches the scintillation crystal. The distribution of hits on the scintillation crystal follows a Poisson distribution, as depicted in Fig. 1.1. The Poisson distribution is approached with a Gaussian for sufficiently large data sets. The pixel value corresponding to the centroid of the Gaussian fit is considered the most accurate representation of the tracer particle's projected position and is used for the reconstruction. The distance between the slit collimator and the scintillation crystal can be adjusted to control the magnification of the projection.

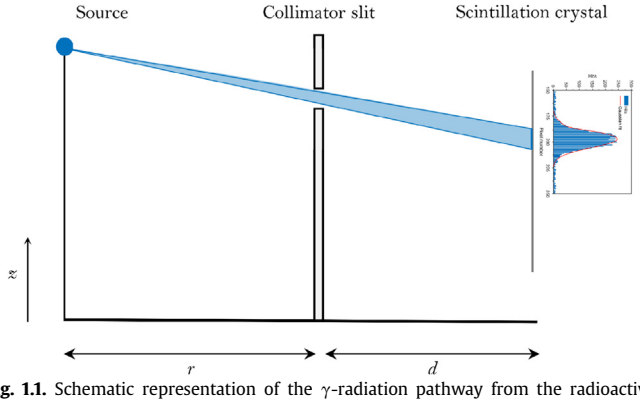

Fig. 1.1. Schematic representation of the γ-radiation pathway from the radioactive tracer particle, through the slit collimator to the scintillation crystal. The letter 'r' and 'd' represent the tracer particle to slit collimator and slit collimator to scintillation crystal distance, respectively.

2 Calibration setup

To calibrate the spatial geometry of the RPT setup, a constrained non-linear least squares optimization algorithm was employed. This algorithm aims to minimize the spatial error between the true position of the tracer particle and the reconstructed position obtained from the RPT system. The algorithm adjusts the geometry values within specified upper and lower bounds (set at 50 mm) and returns the calibrated geometry. The calibrated spatial orientation of the three detectors is shown in Fig. 2.1. A comparison with the hand-measured geometry reveals that each detector in the calibrated setup has undergone a slight translation and rotation, effectively correcting for measurement inaccuracies. The calibration process leads to significantly improved accuracy and precision in the reconstruction of the tracer particle position.

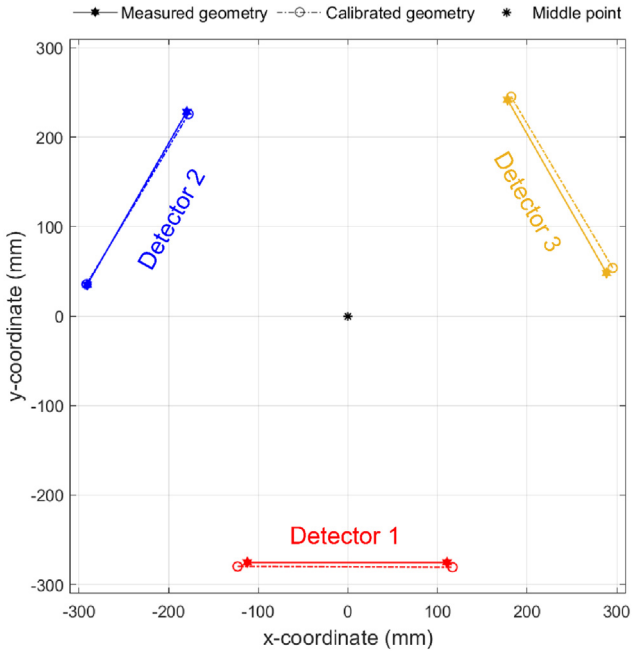

Fig. 2.1. Spatial orientation of the three detectors relative to the middle point in the hand-measured geometry and calibrated geometry.

References

Alizadeh, E., Dubé, O., Bertrand, F., & Chaouki, J. (2013). Characterization of mixing and size segregation in a rotating drum by a particle tracking method. *AIChE Journal, 59*, 1894–1905.

Caracotsios, M. (1992). Theoretical modelling of amoco's gas phase horizontal stirred bed reactor for the manufacturing of polypropylene resins. *Chemical Engineering Science, 47*, 2591–2596.

Chaouki, J., Larachi, F., & Duduković, M. P. (1997). Noninvasive tomographic and velocimetric monitoring of multiphase flows. *Industrial & Engineering Chemistry Research, 36*, 4476–4503.

Devanathan, N., Moslemian, D., & Dudukovic, M. P. (1990). Flow mapping in bubble columns using carpt. *Chemical Engineering Science, 45*, 2285–2291.

Dittrich, C. J., & Mutsers, S. M. P. (2007). On the residence time distribution in reactors with non-uniform velocity profiles: The horizontal stirred bed reactor for polypropylene production. *Chemical Engineering Science, 62*, 5777–5793.

Dubé, O., Dubé, D., Chaouki, J., & Bertrand, F. (2014). Optimization of detector positioning in the radioactive particle tracking technique. *Applied Radiation and Isotopes, 89*, 109–124.

Duduković, M. (2000). Opaque multiphase reactors: Experimentation, modeling and troubleshooting, oil & gas science and Technology – Rev. IFP Éditions Technip oil & gas science and Technology – Rev. *IFP, 55*, 135–158.

F, L., G, K., & J, C. (1994). *A [gamma]-ray detection system for 3-d particle tracking in multiphase reactors*. https://doi.org/10.1016/0168-9002(94)91343-9

Fraguío, M. S., Cassanello, M. C., Larachi, F., Limtrakul, S., & Dudukovic, M. (2007). Classifying flow regimes in three-phase fluidized beds from carpt experiments. *Chemical Engineering Science, 62*, 7523–7529.

Godfroy, L., Larachi, F., Kennedy, G., & Chaouki, J. (1996). *Simultaneous measurement of the 3-d position and velocity of a single radioactive particle in a cfb riser at high velocity*. Beijing, China: Proceedings of CFB V.

Godfroy, L., Larachi, F., Kennedy, G., Grandjean, B., & Chaouki, J. (1997). On-line flow visualization in multiphase reactors using neural networks. *Applied Radiation and Isotopes, 48*, 225–235.

Guha, D., Ramachandran, P. A., & Dudukovic, M. P. (2007). Flow field of suspended solids in a stirred tank reactor by Lagrangian tracking. *Chemical Engineering Science, 62*, 6143–6154.

Holman, B. L., & Tumeh, S. S. (1990). Single-photon emission computed tomography (SPECT): Applications and potential. *JAMA, 263*, 561–564.

Jain, V., Kalo, L., Kumar, D., Pant, H. J., & Upadhyay, R. K. (2017). Experimental and numerical investigation of liquid–solid binary fluidized beds: Radioactive particle tracking technique and dense discrete phase model simulations. *Particuology, 33*, 112–122.

Kalo, L., Pant, H. J., Cassanello, M. C., & Upadhyay, R. K. (2019). Time series analysis of a binary gas-solid conical fluidized bed using radioactive particle tracking (rpt) technique data. *Chemical Engineering Journal, 377*.

Kertzscher, U., Seeger, A., Affeld, K., Goubergrits, L., & Wellnhofer, E. (2004). X-ray based particle tracking velocimetry—a measurement technique for multi-phase flows and flows without optical access. *Flow Measurement and Instrumentation, 15*, 199–206.

Larachi, F., Cassanello, M., Marie, M., Chaouki, J., & Guy, C. (1995). Solids circulation patterns in 3-phase fluidized-beds containing binary-mixtures of particles as inferred from rpt. *Chemical Engineering Research and Design, 73*, 263–268.

Larachi, F., Chaouki, J., & Kennedy, G. D. (1995). 3-d mapping of solids flow fields in multiphase reactors with rpt. *AIChE Journal, 41*, 439–443.

Larachi, F., Lord, E., Chaouki, J., Chavarie, C., & Behie, L. (1995). *Phenomenological study of solids mixing in a binary liquid fluidized bed* (pp. 385–392). Tours, France: Prep Fluidization VIII.

Lin, J. S., Chen, M. M., & Chao, B. T. (1985). A novel radioactive particle tracking facility for measurement of solids motion in gas fluidized beds. *AIChE Journal, 31*, 465–473.

Moslemian, D., Devanathan, N., & Dudukovic, M. P. (1992). Radioactive particle tracking technique for investigation of phase recirculation and turbulence in multiphase systems. *Review of Scientific Instruments, 63*, 4361–4372.

Mostoufi, N., Kenned, G., & Chaouki, J. (2003). Decreasing the sampling time interval in radioactive particle tracking. *Canadian Journal of Chemical Engineering, 81*, 129–133.

Parker, D. J., Hawkesworth, M. R., & Beynon, T. D. (1995). Process applications of emission tomography. *The Chemical Engineering Journal and the Biochemical Engineering Journal, 56*, 109–117.

Rammohan, A. R., Kemoun, A., Al-Dahhan, M. H., & Dudukovic, M. P. (2001). Characterization of single phase flows in stirred tanks via computer automated radioactive particle tracking (carpt). *Chemical Engineering Research and Design, 79*, 831–844.

Rasouli, M., Bertrand, F., & Chaouki, J. (2015). A multiple radioactive particle tracking technique to investigate particulate flows. *AIChE Journal, 61*, 384–394.

Roy, S. (2017). Radiotracer and particle tracking methods, modeling and scale-up. *AIChE Journal, 63*, 314–326.

Roy, S., Kemoun, A., Al-Dahhan, M. H., & Dudukovic, M. P. (2005). Experimental investigation of the hydrodynamics in a liquid–solid riser. *AIChE Journal, 51*, 802–835.

Roy, S., Larachi, F., Al-Dahhan, M. H., & Duduković, M. P. (2002). Optimal design of radioactive particle tracking experiments for flow mapping in opaque multiphase reactors. *Applied Radiation and Isotopes, 56*, 485–503.

Roy, D., Larachi, F., Legros, R., & Chaouki, J. (1994). A study of solid behavior in spouted beds using 3-d particle tracking. *Canadian Journal of Chemical Engineering, 72*, 945–952.

Seeger, A., Kertzscher, U., Affeld, K., & Wellnhofer, E. (2003). Measurement of the local velocity of the solid phase and the local solid hold-up in a three-phase flow by x-ray based particle tracking velocimetry (xptv). *Chemical Engineering Science, 58*, 1721–1729.

Stellema, C. S., Vlek, J., Mudde, R. F., de Goeij, J. J. M., & van den Bleek, C. M. (1998). Development of an improved positron emission particle tracking system. *Nuclear Instruments and Methods in Physics Research Section A: Accelerators, Spectrometers, Detectors and Associated Equipment, 404*, 334–348.

Upadhyay, R. K., Pant, H. J., & Roy, S. (2019). Experimental validation of design and performance parameters of radioactive particle tracking (rpt) experimentation. *Applied Radiation and Isotopes, 153*, 108814.

Windows-Yule, C., Seville, J., Ingram, A., & Parker, D. (2020). Positron emission particle tracking of granular flows. *Annual Review of Chemical and Biomolecular Engineering, 11*, 367–396. PMID: 32228041.

Xi, Y., Chen, Q., & You, C. (2015). Flow characteristics of biomass particles in a horizontal stirred bed reactor: Part ii. modeling studies on particle residence time distribution and axial mixing. *Powder Technology, 269*, 585–595.

Yadav, A., Gaurav, T. K., Pant, H. J., & Roy, S. (2020). Machine learning based position-rendering algorithms for radioactive particle tracking experimentation. *AIChE Journal, 66*.

Yadav, A., Ramteke, M., Pant, H. J., & Roy, S. (2017). Monte Carlo real coded genetic algorithm (mc-rga) for radioactive particle tracking (rpt) experimentation. *AIChE Journal, 63*, 2850–2863.